Nanoscale

COMMUNICATION

Er³⁺-to-Yb³⁺ and Pr³⁺-to-Yb³⁺ energy transfer for highly efficient near-infrared cryogenic optical temperature sensing†

Anna M. Kaczmarek, [ID] *[a] Mariusz K. Kaczmarek[b] and Rik Van Deun [ID] *[a]

Here, the very high thermal sensing capability of Er³⁺,Yb³⁺ doped LaF₃ nanoparticles, where Er³⁺-to-Yb³⁺ energy transfer is used, is reported. Also Pr³⁺,Yb³⁺ doped LaF₃ nanoparticles, with Pr³⁺-to-Yb³⁺ energy transfer, showed temperature sensing in the same temperature regime, but with lower performance. The investigated Er³⁺,Yb³⁺ doped LaF₃ nanoparticles show a remarkably high relative sensitivity S_r of up to 6.6092% K⁻¹ (at 15 K) in the near-infrared (NIR) region, in the cryogenic (15–105 K) temperature region opening a whole new thermometric system suitable for advanced applications in the very low temperature ranges. To date reports on NIR cryogenic sensors have been very scarce.

The downshifting and upconversion emissions of trivalent lanthanide (Ln³⁺) materials (*e.g.* phosphors, complexes, and MOFs) have been extensively explored for use in optical temperature sensing.[1–12] The Er³⁺,Yb³⁺ system has been greatly explored for temperature sensors based on upconversion, mostly showing good performance in the high temperature regime.[4,13–16] Also there have been some reports on Pr³⁺ based thermometers, which also show good performance at high temperatures, but they are rather rare.[17,18] Most thermometer materials operating in the NIR region are based on single ion materials. For example Benayas *et al.* reported Nd³⁺-doped Y₃Al₅O₁₂ nanoparticles where the two Stark sublevels of the ⁴F₃/₂ → ⁴I₉/₂ transition were used for ratiometric sensing.[19] Wawrzynczyk *et al.* reported Nd³⁺-doped NaYF₄ nanoparticles, and here also the temperature evolution and sensing properties were realized by measuring the intensity ratio of the two Stark sublevels of the ⁴F₃/₂ multiplet in the Nd³⁺ ion.[20] More recently Marciniak *et al.* have reported exciting results of

a new type of luminescence thermometer – LiLaP₄O₁₂:Cr,Nd, which showed NIR sensing in the physiological range reaching 4.89% K⁻¹, which was one to two orders of magnitude higher than most reported NIR sensors.[21] Optical temperature sensing in the cryogenic region is very important for applications in energy storage industries and aerospace. To date only a few reported materials have showed good temperature sensing in the cryogenic region, such as [Tb₀.₉₁₄Eu₀.₀₈₆₂(pda)₃(H₂O)]·2H₂O measured from 10–325 K, showing S_r of 5.96% K⁻¹ (at 25 K), Tb₀.₉₅Eu₀.₀₅HL (H₄L = 5-hydroxy-1,2,4-benzenetricarboxylic acid) exhibiting S_r of 31% at 4 K or 1.6% Eu³⁺ doped [Tb₈(MoO₄)₂(H₂O)₂₆(Mo₇O₂₄)₈]²⁸⁻ showing S_r of 4.76% K⁻¹ (at 50 K).[3,5,7] Not much work can be found on NIR sensors operating in the cryogenic temperature regime. Very recently Ananias *et al.* have reported on a NIR thermometer based on Er³⁺,Yb³⁺:Na₂K[Lu₃Si₆O₁₈], where Yb³⁺-to-Er³⁺ energy transfer was observed and the material was used as a cryogenic thermometer (S_r = 2.6% K⁻¹ at 26.8 K).[22] Compared to MOFs and POMs, purely inorganic materials are much easier to prepare, significantly more stable, and highly processable (when at nanosize). In this communication we report Er³⁺,Yb³⁺ and Pr³⁺,Yb³⁺ doped LaF₃ nanoparticles, using a well-known low phonon fluoride matrix, where the energy is transferred from Er³⁺/Pr³⁺ to Yb³⁺ yielding S_r = 6.6092% K⁻¹ (at 15 K) for Er³⁺,Yb³⁺:LaF₃ and S_r = 1.0839% K⁻¹ (at 25 K) for Pr³⁺,Yb³⁺:LaF₃, which are very high values for the NIR region and one of the few reports of NIR cryogenic optical sensors.

The materials were fully characterized by powder X-ray diffraction (PXRD), X-ray fluorescence (XRF), transmission electron microscopy (TEM), and luminescence spectroscopy.

The powder XRD patterns of Er³⁺,Yb³⁺:LaF₃ and Pr³⁺,Yb³⁺:LaF₃ (after heat treatment at 600 °C) could be well matched to the standard PDF No. 32-0483 (Fig. 1). XRF analysis was performed to determine the exact doping percentage of the doped lanthanide ions in the LaF₃ materials and it was found to be 2.96% Er, 1.57% Yb and 95.47% La for Er³⁺,Yb³⁺:LaF₃ and 2.20% Pr, 1.43% Yb, and 96.37% La for Pr³⁺,Yb³⁺:LaF₃, respectively. In the synthesis we used 3% Er/Pr, 1.5% Yb and 95.5%

[a]L³ – Luminescent Lanthanide Lab, Department of Chemistry, Ghent University, Krijgslaan 281-S3, B-9000 Ghent, Belgium. E-mail: Rik.VanDeun@UGent.be, Anna.Kaczmarek@UGent.be
*[b]Institute of Mechanics and Applied Science, Kazimierz Wielki University in Bydgoszcz, Kopernika 1, 85-074 Bydgoszcz, Poland*
†Electronic supplementary information (ESI) available: Additional luminescence data. See DOI: 10.1039/c8nr08348g
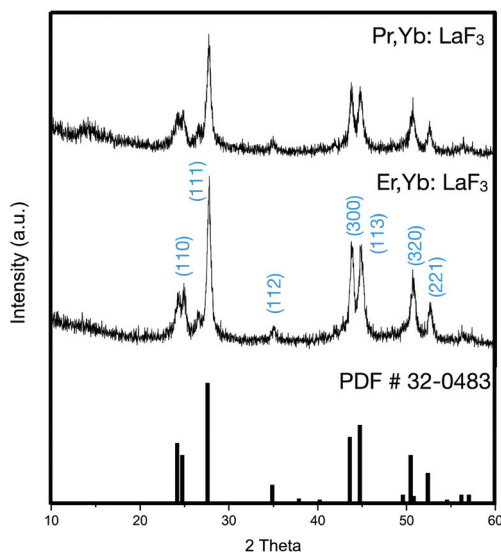
Fig. 1 Powder XRD patterns of 2.96% Er^{3+},1.57% Yb^{3+}:LaF_3 and 2.20% Pr,1.45% Yb:LaF_3 compared to the standard powder XRD pattern of LaF_3 (PDF # 32-0483).

La, therefore the exact percentages determined by XRF were reasonably comparable with the amounts of lanthanide ions used in the synthesis. These particles were analysed by TEM to obtain information about their morphology (Fig. 2a and b). The obtained nanoparticles were a mixture of spherical and cubic particles and were of around 10–20 nm on average in size. Due to the high temperature heat treatment process they showed some tendency to aggregate, but single particles could still be identified (Fig. 2c and d). On average the particles slightly increased in size usually up to 20–30 nm.
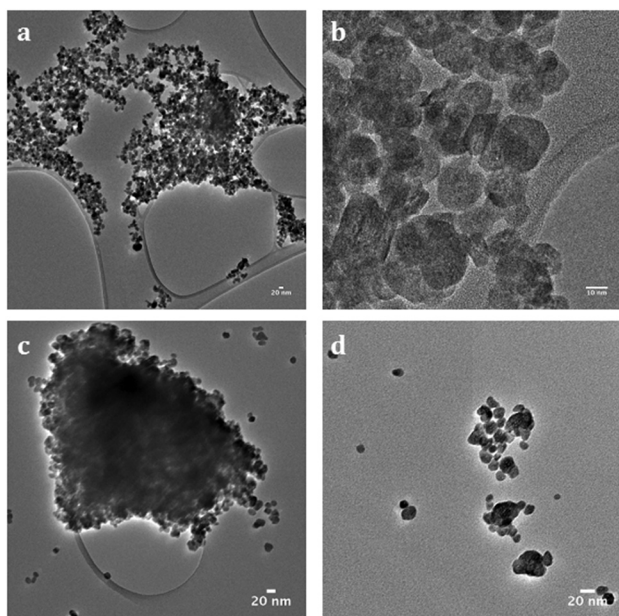
Fig. 2 TEM images of (a, b) the 2.96% Er^{3+},1.57% Yb^{3+}:LaF_3 nanoparticles before heat treatment and (c, d) after heat treatment at 600 °C.

Luminescence at room temperature and temperature dependent measurements were performed on the heat-treated Er^{3+},Yb^{3+}:LaF_3 and Pr^{3+},Yb^{3+}:LaF_3 samples. The excitation spectrum of Er^{3+},Yb^{3+}:LaF_3 recorded at RT is shown in Fig. S1.† All of the sharp f–f peaks could be assigned to well-known Er^{3+} transitions peaks (Table S1†). The excitation spectrum was also recorded at 15 K and showed stronger intensity as well as some differences in the observed peaks (Fig. S2 and Table S2†). The sample was excited at 377.9 nm (into the $^4G_{11/2} \leftarrow {}^4I_{15/2}$ transition) at RT and the obtained NIR emission spectrum is shown in Fig. S3.† At 988.3 nm (10 118 cm^{-1}) the $^2F_{5/2} \rightarrow {}^2F_{7/2}$ transition of Yb^{3+} is visible and at 1539.8 nm (6494 cm^{-1}) the $^4I_{13/2} \rightarrow {}^4I_{15/2}$ transition of Er^{3+} is visible, respectively. The performed luminescence measurements give convincing evidence of the energy transfer from Er^{3+} to Yb^{3+}. It is very likely that the observed energy transfer in this sample and the Pr^{3+},Yb^{3+}:LaF_3 material is a downconversion process as it has previously been reported that these lanthanide pairs (Pr/Yb, Er/Yb) and particularly in the LaF_3 matrix as well as in other inorganic matrixes show downconversion.[23–25] This would show that the downconversion process can also be used for designing very efficient NIR optical temperature sensors.

The excitation source and/or the detector often affect temperature-sensing measurements based on a single transition band.[26,27] Thermometers based on the intensity ratio of two transitions, preferably well separated to ensure the material has a good signal discriminability, overcome these drawbacks. In the Er^{3+},Yb^{3+} co-doped sample and the Pr^{3+},Yb^{3+} co-doped sample, a big advantage is the good separation of the observed peaks. The thermometric parameter Δ can be expressed using the following equations (1)–(4).

$$\Delta = \frac{I_1}{I_2} \tag{1}$$

$$\Delta = \alpha \exp\left(-\frac{\Delta E}{k_B T}\right) \tag{2}$$

$$\Delta = \frac{\Delta_0}{1 + \alpha \exp\left(-\frac{\Delta E}{k_B T}\right)} \tag{3}$$

$$\Delta = \frac{\Delta_0}{1 + \alpha_1 \exp\left(-\frac{\Delta E_1}{k_B T}\right) + \alpha_2 \exp\left(-\frac{\Delta E_2}{k_B T}\right)} \tag{4}$$

where I_1 and I_2 are the maximum intensity of the peaks at the selected wavelengths; Δ_0 is the thermometric parameter at $T = 0$ K; $\alpha = W_0/W_R$ is the ratio between the nonradiative rates (W_0 is at $T = 0$ K) and radiative rates (W_R); K_B is the Boltzmann constant; T is the absolute temperature (K); and ΔE is the activation energy of the non-radiative process.[7] For dual-center thermometers (as is the case presented in this paper), the most commonly employed equation used for the conversion of luminescence intensity to temperature is eqn (3). However, in some cases when two non-radiative processes take place eqn (4) should be used.[12]

The absolute sensitivity S_a and the relative sensitivity S_r can be expressed using eqn (5) and (6).

$$S_a = \left| \frac{\partial \Delta}{\partial T} \right| \tag{5}$$

$$S_r = 100\% \times \left| \frac{1}{\Delta} \frac{\partial \Delta}{\partial T} \right| \tag{6}$$

S_r is a more important parameter compared to S_a for quantifying and comparing the sensitivity of different thermometers as S_a is strongly dependent on the sample features and the experimental device. S_r indicates the relative change of the thermometric parameter per degree of temperature change (% K^{-1}). All of the thermometric parameters in this work were calculated using the TeSen MATLAB based software developed by us.[28]

The emission map of 2.96% Er^{3+},1.57% Yb^{3+}:LaF_3 was recorded over a 15–105 K range and is shown in Fig. 3a. With an increase in temperature the intensity of both the $^2F_{5/2} \rightarrow$ $^2F_{7/2}$ transition of Yb^{3+} and the $^4I_{13/2} \rightarrow$ $^4I_{15/2}$ transition of Er^{3+} decreases. As the measurement data consist of signals of interest, but also contain baseline offset and noise, and in some cases even measurement artifacts, it is therefore important, especially when measurements are recorded in the NIR region (where the signal is low compared to noise), to properly treat the data before performing calculations to assess the thermometer performance.[27] Such pre-processing includes reducing signal noise, removing baseline offset and other instrumental artifacts. This pre-processing can heavily influence the final results of the calculations. For our Er^{3+},Yb^{3+}:LaF_3 material we have performed baseline offset removal and smoothing (5 point S-G smoothing) of the emission peaks and showed its influence of the experimental Δ points at different temperatures. This is shown in Fig. S4–S6.† Generally discussion on the influence of data pre-processing on the thermometric parameter value is currently lacking in most papers on optical sensors, yet it has an important effect on the calculation outcome.

After data pre-processing, based on the peak maxima as well as the integrated areas under the peak, the experimental thermometric parameters were determined ($I_{988.3}/I_{1539.8}$). They could be well fitted employing eqn (4) yielding $R^2 = 0.99471$ (for peak maxima) and $R^2 = 0.99802$ (for integrated area under the peaks) (see Fig. 3b). For calculations based on the peak maxima the equation fit yielded $\Delta_0 = 7.37$, $\alpha_1 = 35.30$, $\Delta E_1 =$
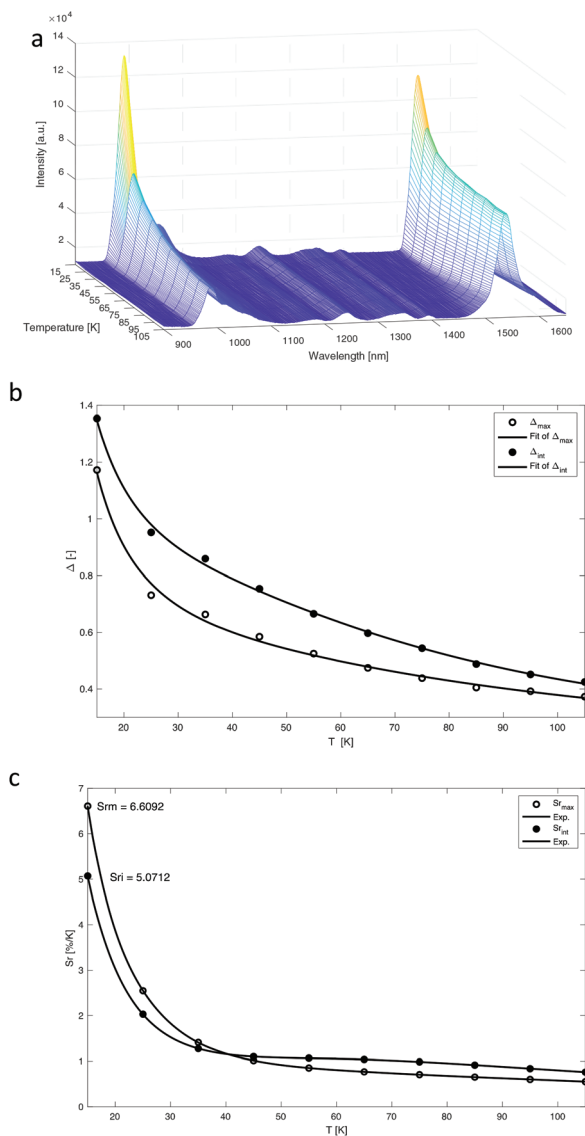
Fig. 3 (a) Emission map of spectra recorded at 15–105 K for 2.96% Er^{3+},1.57% Yb^{3+}:LaF_3; (b) plot presenting the calibration curves for compound Er^{3+},Yb^{3+}:LaF_3 when eqn (4) is employed. The points show the experimental Δ parameters and the solid lines show the best fit of the experimental points using eqn (4). The opened points represent Δ calculated from the peak maxima, whereas the filled points represent the Δ calculated from the integrated areas under the peaks; and (c) plot presenting the relative sensitivity S_r values at varied temperatures (15–105 K) for 2.96% Er^{3+},1.57% Yb^{3+}:LaF_3. The opened points show results for the peak maxima, whereas the filled points show results for the integrated areas under the peaks. The solid lines are a guide to the eye.
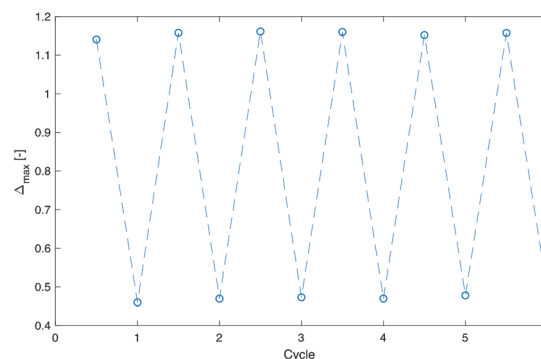
Fig. 4 Plot showing heating, cooling and reheating tests of 2.96% Er^{3+},1.57% Yb^{3+}:LaF_3 when observed at the peak maximum. The material showed stability from 96.5%–98.75%.

Table 1 Overview of the relative sensitivity S_r (highest value) for the chosen recently reported materials showing performance in the cryogenic region

Material	Emission	Max. S_r [% K^{-1}]	T_m (K)	Ref.
$[(Tb_{0.914}Eu_{0.0860}(pda)_3(H_2O)]\cdot 2H_2O$	Visible	5.96	25	3
$Tb_{0.95}Eu_{0.05}HY$	Visible	31.0	4	5
$[Tb_8(MoO_4)_2(H_2O)_{26}(Mo_7O_{24})_8]^{28-}$	Visible	4.76	50	7
$Na_2K[(Lu_{0.75}Yb_{0.20}Er_{0.05})_3Si_6O_{18}]$	NIR	2.60	26.8	22
$Eu_{0.02}Gd_{0.98}(dsb)$	Visible	7.14	65	29
$[Eu_{0.102}Tb_{0.898}(notpH_4)(NO_3)(H_2O)]\cdot 8H_2O$	Visible	3.90	38	30
2.96% Er^{3+},1.57% Yb^{3+}:LaF_3	NIR	6.61	15	This work
2.20% Pr^{3+},1.45% Yb^{3+}:LaF_3	NIR	1.08	25	This work

152.09 cm^{-1}, $\alpha_2 = 17.33$, and $\Delta E_2 = 12.27$ cm^{-1}. For calculations based on the integrated areas under the peaks the equation fit yielded $\Delta_0 = 5.70$, $\alpha_1 = 35.30$, $\Delta E_1 = 141.87$ cm^{-1}, $\alpha_2 = 8.7499$, and $\Delta E_2 = 10.38$ cm^{-1}. The larger non-radiative deactivation energy (ΔE_1) probably involves the $^4I_{11/2}$ level of Er^{3+} and the $^2F_{5/2}$ level of Yb^{3+}. The smaller non-radiative deactivation energy (ΔE_2) most likely involves non-radiative deactivation through the multiple Er^{3+} local sites (Er^{3+}–Er^{3+} energy migration). In Fig. S7† and Fig. 3c the S_a and S_r values, calculated at different temperatures, have been presented, respectively. The maximum value of S_a was 0.076872 K^{-1} (at 15 K) for the peak maxima, and 0.068336 K^{-1} (at 15 K) for the integrated areas under the peaks. The maximum S_r value was 6.6092% K^{-1} (at 15 K) for the peak maxima, and 5.0712% K^{-1} (at 15 K) for the integrated areas under the peaks. The S_r values are higher than those previously reported for NIR thermometers, proving their excellent performance. To test the stability of this optical sensor material six cycle tests were performed (Fig. 4). The thermometer showed stability from 96.5%–98.75% when observing the peak maximum.

Additionally the 2.20% Pr^{3+},1.45% Yb^{3+}:LaF_3 sample was also investigated for use as a NIR cryogenic sensor. A maximum S_r value of 1.0839% K^{-1} was obtained at 25 K when calculated based on the peak maxima, whereas a maximum S_r of 0.528145% K^{-1} was obtained at 15 K when calculated based on the integrated areas under the peaks. These values are lower than those for the 2.96% Er^{3+},1.57% Yb^{3+}:LaF_3 material, yet still higher than those of most previously reported NIR temperature sensors to date, and interestingly they show a similar trend of being sensitive in the cryogenic region. The results for this sample are shown in ESI Fig. S8–S13.† In Table 1 we have overviewed known cryogenic sensors.

In this work we have reported the excellent cryogenic thermometer properties of a Er^{3+}-to-Yb^{3+} energy transfer system in the 2.96% Er^{3+},1.57% Yb^{3+}:LaF_3 material ($S_r > 6\%$ K^{-1}). We also investigated the 2.20% Pr^{3+},1.45% Yb^{3+}:LaF_3 material, which shows lower relative sensitivity ($S_r > 1\%$ K^{-1}), yet it is also sensitive in the cryogenic range showing the usefulness of employing Er^{3+}-to-Yb^{3+} and Pr^{3+}-to-Yb^{3+} energy transfer in the very low temperature regime. Such systems have been rarely considered for use in optical temperature sensors to date, yet they allow one to obtain very good relative sensitivity in the NIR range in the cryogenic temperature region, as well as very good stability during cycle tests. The obtained results are one order of magnitude higher than that of most reported NIR temperature sensors. Additionally NIR cryogenic sensing is very scarcely reported.

Conflicts of interest

There are no conflicts to declare.

Acknowledgements

References

1 Y. Ciu, H. Xu, Y. Yue, Z. Guo, J. Yu, Z. Chen, J. Gao, Y. Yang, G. Qian and B. Chen, *J. Am. Chem. Soc.*, 2012, **134**, 3979–3982.

2 D. Ananias, C. D. S. Brites, L. D. Carlos and J. Rocha, *Eur. J. Inorg. Chem.*, 2016, 1967.

3 Z. Wang, D. Ananias, A. Carne-Sanchez, C. D. S. Brites, I. Imaz, D. Maspoch, J. Rocha and L. D. Carlos, *Adv. Funct. Mater.*, 2015, **25**, 2824–2830.

4 R. G. Geitenbeek, P. T. Prins, W. Albrecht, A. van Blaaderen, B. M. Weckhuysen and A. Meijerink, *J. Phys. Chem. C*, 2017, **121**, 3503–3510.

5 X. Liu, S. Akerboom, M. de Jong, I. Mutikainen, S. Tanse, A. Meijerink and E. Bouwman, *Inorg. Chem.*, 2015, **54**, 11323–11329.

6 A. M. Kaczmarek, Y.-Y. Liu, C. Wang, B. Laforce, L. Vincze, P. Van Der Voort and R. Van Deun, *Dalton Trans.*, 2017, **46**, 12717–12723.

7 A. M. Kaczmarek, J. Liu, B. Laforce, L. Vincze, K. Van Hecke and R. Van Deun, *Dalton Trans.*, 2017, **46**, 5781–5785.

8 L. Marciniak, K. Prorok and A. Bednarkiewicz, *J. Mater. Chem. C*, 2017, **5**, 7890–7897.

9 Y. Ciu, R. Song, J. Yu, M. Liu, Z. Wang, C. Wu, Y. Yang, Z. Wang, B. Chen and G. Qian, *Adv. Mater.*, 2015, **27**, 1420–1425.

10 L. Marciniak, A. Bednarkiewicz, J. Drabiak, K. Trejgis and W. Strek, *Phys. Chem. Chem. Phys.*, 2017, **19**, 7343–7351.

11 L. Li, Y. Zhu, X. Zhou, C. D. S. Brites, D. Ananias, Z. Lin, F. A. Almeida Paz, J. Rocha, W. Huang and L. D. Carlos, *Adv. Funct. Mater.*, 2016, **26**, 8677–8684.

12 A. M. Kaczmarek, *J. Mater. Chem. C*, 2018, **6**, 5916–5925.

13 G. Zhang, Q. Qiang, S. Du and Y. Wang, *RSC Adv.*, 2018, **8**, 9512–9518.

14 D. T. Klier and M. U. Kumke, *J. Phys. Chem. C*, 2015, **119**, 3363–3373.

15 X. Yang, Z. Fu, Y. Yang, C. Zhang, Z. Wu and T. Sheng, *J. Am. Ceram. Soc.*, 2015, 1–6.

16 S. Hao, G. Chen and C. Yang, *Theranostics*, 2013, **3**, 331–345.

17 M. S. Pudovkin, O. A. Morozov, V. V. Pavlov, S. L. Korableva, E. V. Lukinova, Y. N. Osin, V. G. Evtugyn, R. A. Safiullin and V. V. Semashko, *J. Nanomater.*, 2017, 3108586.

18 X. Tang, X. Li, Z. Zou, Z. Ma, J. Zhang, Z. Wang, Z. Ci, D. Wang, S. Peng, H. Li and Y. Wang, *J. Mater. Chem. C*, 2017, **5**, 10369–10374.

19 A. Benayas, B. del Rosal, A. Perez-Delgado, K. Santacruz-Gomez, D. Jaque, G. A. Hirata and F. Vetrone, *Adv. Opt. Mater.*, 2015, **3**, 687–694.

20 D. Wawrzynczyk, A. Bednarkiewicz, M. Nyk, W. Strek and M. Samoc, *Nanoscale*, 2012, **4**, 6959–6961.

21 L. Marciniak, A. Bednarkiewicz and W. Strek, *Sens. Actuators, B*, 2017, **238**, 381–386.

22 D. Ananias, F. A. Almeida Paz, L. D. Carlos and J. Rocha, *Chem. – Eur. J.*, 2018, **24**, 11926–11935.

23 K. Deng, X. Wei, X. Wang, Y. Chen and M. Yin, *Appl. Phys. B*, 2011, **102**, 555–558.

24 L. Aarts, S. Jaeqx, B. M. van der Ende and A. Meijerink, *J. Lumin.*, 2011, **131**, 608–613.

25 L. Aarts, B. M. van der Ende and A. Meijerink, *J. Appl. Phys.*, 2009, **106**, 023522.

26 L. D. Carlos and F. Palacio, *Thermometry at the Nanoscale: Techniques and Selected Applications*, Royal Society of Chemistry, Oxfordshire, 2016.

27 M. D. Dramicanin, *Luminescence Thermometry*, first edition, Woodhead Publishing, 2018.

28 A. M. Kaczmarek, R. Van Deun and M. K. Kaczmarek, *Sens. Actuators, B*, 2018, **273**, 696–702.

29 R. F. D'Vries, S. Alvarez-Garcia, N. Snejko, L. E. Bausa, E. Gutierrez-Puebla, A. de Andres and M. A. Monge, *J. Mater. Chem. C*, 2013, **1**, 6316–6324.

30 M. Ren, C. D. S. Brites, S.-S. Bao, R. A. S. Ferreira, L.-M. Zheng and L. D. Carlos, *J. Mater. Chem. C*, 2015, **3**, 8480–8484.